Research Article | Vol. 34, No. 8 / 20 Apr 2026 / Optics Express 15233
Optics EXPRESS

Ultrafast change of optical polarization predicted for XUV-irradiated diamond

Sebastião Antunes,[1,2,3,*] Flavio Capotondi,[4] Konrad J. Kapcia,[1,5] Vladimir Lipp,[1,2,6] and Beata Ziaja[1,2]

[1]Center for Free-Electron Laser Science CFEL, Deutsches Elektronen-Synchrotron DESY, Notkestr. 85, 22607 Hamburg, Germany
[2]Institute of Nuclear Physics, Polish Academy of Sciences, Radzikowskiego 152, 31-342 Kraków, Poland
[3]Max Planck Institute for the Structure and Dynamics of Matter, Hamburg, Germany
[4]Elettra-Sincrotrone Trieste S.C.p.A, 34149 Trieste, Basovizza, Italy
[5]Institute of Spintronics and Quantum Information, Faculty of Physics and Astronomy, Adam Mickiewicz University in Poznań, Uniwersytetu Poznańskiego 2, PL-61614 Poznań, Poland
[6]European XFEL, Holzkoppel 4, 22869 Schenefeld, Germany
*sebastiao.antunes@desy.de

Abstract: The principle behind light-induced switching, which is used in modern electronic devices, is the modulation of a light signal in an externally modified medium. This allows for real-time control of the signal's phase, amplitude, or polarization. In this study, we theoretically examine transient changes in the optical polarization of wide-bandgap semiconductors irradiated by femtosecond XUV pulses to explore their potential applications in optical switching, using diamond as an example. Specifically, we observe that at a certain combination of XUV pulse parameters, an ultrafast change in the polarization angle can be triggered in diamond. These results suggest a promising approach to reversibly modulate the optical polarization in wide-bandgap semiconductors on a 100 fs timescale.

Published by Optica Publishing Group under the terms of the Creative Commons Attribution 4.0 License. Further distribution of this work must maintain attribution to the author(s) and the published article's title, journal citation, and DOI.

1. Introduction

Light-induced switching is pivotal for many modern electronic systems. For example, various information systems utilize switching of the electrical signal between the "on" and "off" states by radio-frequency electromagnetic fields on nanosecond timescales. This enables information processing at a rate up to a gigahertz [1]. Applying photons as alternative information carriers offers a route to decrease the switching time down to femtoseconds [2].

The principle behind light-induced switching is the modulation of a light signal within a medium whose optical properties are being transiently altered by an external stimulus – most often by another light pulse. Such modulation allows for a real-time control of the signal's phase, amplitude, or polarization, and can be employed for data encoding, all-optical signal processing, and optical recording [2,3]. Polarization-controlled elements are also critical for laser systems and photonic circuits; however, conventional electron-triggered devices are inherently limited in their modulation rate [3].

The key performance parameters typically quoted for optical switching are the switching time and the switching efficiency (which determine the achievable modulation bandwidth and the signal-to-noise ratio), as well as the control power and the device footprint [4]. Simultaneous optimization of these quantities towards femtosecond response, high efficiency, low control power, and nanoscale integration remains a major challenge for optical computing and ultrafast communication [2,5].

#585149 https://doi.org/10.1364/OE.585149
Journal © 2026 Received 18 Nov 2025; revised 24 Mar 2026; accepted 6 Apr 2026; published 15 Apr 2026

Optics EXPRESS

Table 1 summarizes typical performance parameters for several established optical switching systems. For amplitude modulation, a subpicosecond switching can be reached with a control power on the order of tens of GWcm^{-2}. Lowering the control power to a few GWcm^{-2} increases the response timescale to picoseconds. For metamaterials, the switching can be pushed down towards femtoseconds, however, the approach efficiency then considerably decreases. For polarization modulation, the demonstrated switching times lie between 1 and 10 ps, with the respective control power ranging from a few to tens of GWcm^{-2}. The polarization angle then changes between 20% and 60%, assuming the maximal possible rotation to be 90°.

Table 1. An overview of the representative optical switching approaches and their characteristic performance parameters including transmission, *T*, reflection, *R*, and the polarization angle, α

Modulation of	Working Principle	Control Power	Switching Time	Efficiency	Ref.
Amplitude	Photonic Crystals	70 kWcm^{-2}	18 ps	$\Delta T/T$>80%	[2]
	Metamaterials	65 GWcm^{-2}	<100 fs	$\Delta T/T$>40%	[2]
	Microring Resonators	2 GWcm^{-2}	15 ps	$\Delta T/T$>70%	[2]
	Surface Plasmon Polaritons	6 mWcm^{-2}	63 ps	$\Delta T/T \approx 99\%$	[2]
		1 GWcm^{-2}	1 ps	$\Delta R/R \approx 20\%$	[6]
Polarization	Plasmonic Grating	1.4 GWcm^{-2}	<1 ps	$\Delta\alpha = 19°$	[3]
	Metamaterials	16 GWcm^{-2}	10 ps	$\Delta\alpha = 60°$	[7]

So far, the majority of the existing studies have focused on the infrared (IR) or the visible excitation of the signal-modifying media [2], applying nanostructured samples and relying on the nonlinear or the resonant enhancement of the signal in them. Recently, ultrafast polarization switching has also been demonstrated in plasmonic metasurfaces at sub-picosecond timescales and at a moderate control power [4]. Considering amplitude modulation, attosecond four-wave-mixing schemes extended the switching concept to the XUV regime, albeit in the gas phase [8]. In addition, Ref. [1] demonstrated that bulk dielectrics can exhibit sub-fs switching of reflection and transmission while driven by strong-field light pulses, highlighting the feasibility of purely electronically driven optical switching.

In this study, we explore a scheme for the modification of light signal in an XUV excited bulk semiconductor in which the ultrafast polarization response arises from the electronic kinetics within the wide-bandgap material. On the example of diamond, we investigate how femtosecond XUV excitation transiently modifies refractive and absorptive components of the complex refractive index, and how this affects the polarization of an infrared signal. In particular, at a certain set of XUV parameters we observe a several-degree deep decrease and the following "recovery" of the reflected polarization angle within ~ 100 fs, i.e., much faster than the intrinsic carrier relaxation time, e.g., [9]. This reveals a reversible mechanism for a polarization angle change that does not rely on a structural modification or a resonant enhancement of the signal-modifying medium. Owing to diamond's radiation hardness, a control fluence in a range between the hundreds of GWcm^{-2} up to a TWcm^{-2} can be applied without causing structural damage. While the present study focuses on an ambient single-crystal diamond, it can stimulate further investigations towards possible optimization of the control fluence through tailored structures.

The paper is organized as follows. First, the simulation framework and the methodology used to model XUV excitation in semiconductors and to compute their transient optical properties is introduced. Afterwards, the predictions on the evolution of the complex refractive index, the reflectivity, and the resulting polarization rotation for varying absorbed doses and probe (signal) pulse parameters are presented, identifying the regime in which a 100-fs polarization change occurs. Finally, our conclusions are listed.

Optics EXPRESS

2. Modeling XUV irradiation of materials

2.1. Introducing the simulation tool, XTANT

Transient optical properties of XUV irradiated diamond will be computed in this study, using our in-house code XTANT [10–12]. This is a hybrid simulation tool that has been developed since 2013 to investigate X-ray induced electronic and structural transitions in solids. It comprises different interacting modules, namely: (i) Monte Carlo module to model electron and deep-hole kinetics, (ii) transferable tight binding module to describe changing band structure in irradiated solids, (iii) molecular dynamics module to follow nuclei movements, and (iv) Boltzmann collision integral module to describe electron-ion coupling. The code can treat predominant processes that occur in the material during and after its irradiation. The validity of XTANT predictions has been confirmed by their comparison with various experimental data. For example, in [13], the code was successfully applied to explain the behaviour of the experimentally observed transient optical transmission through a layer of XUV-irradiated diamond during its phase transition to a graphite state.

In Fig. 1, we present a schematic overview of X-ray-induced processes in a solid material, and describe how they are modeled with our tool, XTANT. This simulation scheme applies periodic boundary conditions. When a photon is absorbed in the material, it can create a deep-shell hole or a valence-shell hole, releasing a photoelectron. The hole may undergo further decay process such as, e.g., Auger decay, followed by the emission of another electron. The released electrons undergo one or multiple inelastic scatterings (which create secondary electrons) until they loose most of their energy. Both the photoinduced and the subsequent electronic relaxation processes, in which the released electrons participate, are modeled in the XTANT with the Monte Carlo module. Atomistic photo- and electron impact ionization cross sections (or rates) are used in this module.

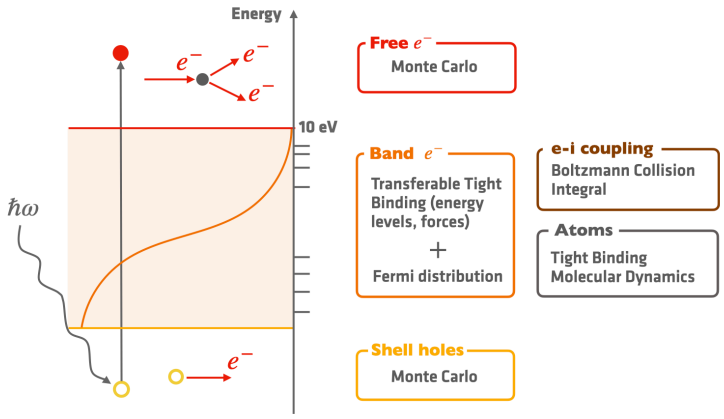

Fig. 1. Schematic representation of the simulation scheme used by the XTANT code

If the energy of an impact electron decreases below a certain energy threshold (in our case, below 10 eV), this electron joins the so called low-energy electron fraction that includes the electrons in the valence band and at the bottom of the conduction band. The low-energy electrons are distributed on the energy levels in these bands that are calculated on-the-fly by the transferable tight-binding module of XTANT. This module also enables to estimate the forces acting on atoms. They are derived from the potential energy surface which is calculated by the transferable tight-binding module at each time step. Atomic trajectories are then followed by solving Newton's equation with the calculated forces. The molecular dynamics module of XTANT is responsible for the calculation of atomic trajectories. Finally, the energy exchange between the electronic and

Optics EXPRESS

the atomic systems is estimated with a Boltzmann collision integral that relies on the knowledge of the electron transition rates between various energy levels and the transient electronic distribution [11].

2.2. Calculation of optical properties with XTANT

Figure 2 shows the scheme used to study transient optical properties of XUV irradiated diamond. The XUV pulse of femtosecond duration arrives at a normal incidence to the sample surface. The infrared probe/signal pulse arrives at the angle, θ, to the surface normal. The initial polarization angle of the optical pulse is denoted as α. For ambient diamond, after the reflection, it changes to α'. During the XUV irradiation, it changes with time as $\alpha'(t)$. Here, $\alpha'(t_0) = \alpha'$, where t_0 denotes the start time of the simulation (before the XUV irradiation begins). The sample thickness, d, corresponds to the XUV attenuation length, λ_{att}, in diamond at a given XUV photon energy. This ensures an approximately uniform in-depth energy distribution in the layer, enabling a straightforward linear conversion between the XUV pulse fluence and the average absorbed dose per atom (see, e.g., [14]).

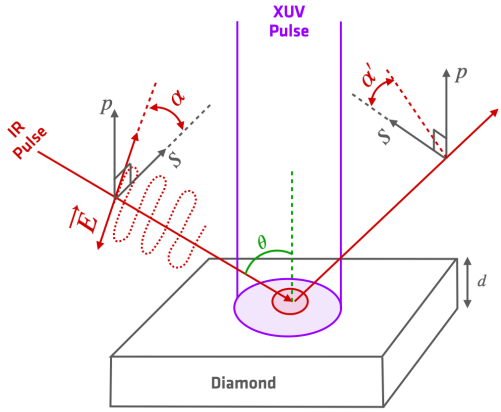

Fig. 2. Schematic of the simulation setup, showing the key parameters used in the current study of XUV-irradiated diamond probed with IR rays.

With XTANT, we can obtain information on the transient optical properties of the irradiated diamond. They change due to the radiation-induced electron excitation in the solid, and, at sufficiently high absorbed doses, also due to the modification of the band structure caused by atomic dislocations. The optical properties can be derived from the dielectric tensor calculated in the random phase approximation (Lindhard approach). Details regarding the procedure can be found in [15]. Since diamond is optically isotropic, the complex dielectric tensor then becomes a scalar, $\epsilon(\omega)$ (with ω being the optical angular frequency), and we can obtain the complex refractive index as:

$$n(\omega) = \tilde{n}(\omega) - i\tilde{k}(\omega) = \sqrt{\varepsilon(\omega)}, \tag{1}$$

where $\tilde{n}$ and $\tilde{k}$ are the real and imaginary part of the complex refractive index, respectively. Knowing them, we can calculate the s- and p-reflectivity coefficients as well as the change of the polarization angle for the reflected signal. The procedure of Airy summation (schematically represented in Fig. 3) enables to sum up contributions from all successive transmissions and reflections [16] affecting a thin layer of diamond crystal (with refracting index n_2), flanked by air on both sides (with refracting indices $n_1 = n_3 \approx 1$). The reflectivity coefficients, $R^{s(p)}$, for

Optics EXPRESS

s(p)-polarization are then calculated as:

$$R^{s(p)} = \left| \frac{r_{12}^{s(p)} + r_{23}^{s(p)} e^{-2i\phi}}{1 + r_{12}^{s(p)} r_{23}^{s(p)} e^{-2i\phi}} \right|^2 = \left| \frac{r_{12}^{s(p)} (1 - e^{-2i\phi})}{1 - (r_{12}^{s(p)})^2 e^{-2i\phi}} \right|^2, \tag{2}$$

where

$$r_{12}^{s} = \frac{n_1 \cos\theta_1 - n_2 \cos\theta_2}{n_1 \cos\theta_1 + n_2 \cos\theta_2}, \; r_{12}^{p} = \frac{n_1 \cos\theta_2 - n_2 \cos\theta_1}{n_1 \cos\theta_2 + n_2 \cos\theta_1}, \phi = \frac{2\pi d}{\lambda} n_2 \cos\theta_2, \tag{3}$$

with d being the thickness of the material layer, λ being the IR wavelength, θ_1 being the angle of incidence, and θ_2 being the angle of refraction. Note that we employed here the fact that s and p light waves are independent of each other if the material is optically isotropic. Finally, we calculate the change of the polarization angle, assuming a linearly polarized signal pulse with the polarization angle, α, arriving at the diamond surface. From Eq. (2), we can estimate the fraction of s- and p-polarization of the signal after reflection. The polarization angle of the reflected pulse, $\alpha'(t)$ can then be calculated from the relation:

$$\tan\alpha'(t) = \frac{R_p(t)}{R_s(t)} \cdot \tan\alpha. \tag{4}$$

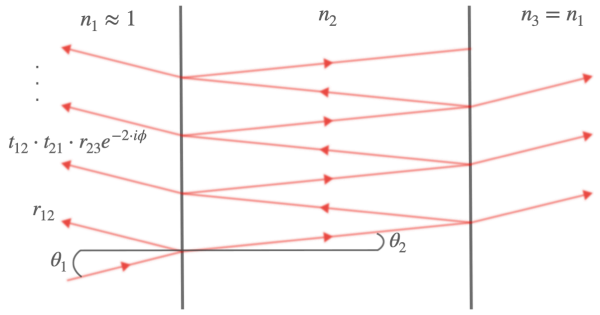

Fig. 3. Principle of Airy's summation.

The change of the polarization of the reflected signal can then be defined as:

$$\Delta\alpha'(t) = \alpha' - \alpha'(t), \tag{5}$$

where, as previously defined, $\alpha' = \alpha'(t_0)$, with t_0 denoting the time of the simulation start, i.e., before XUV irradiation was switched on.

3. Simulation results

3.1. Parameters

Notation for the simulation parameters is adopted from Fig. 2. The duration of XUV is set to 70 fs FWHM, the photon energy equals 50 eV. These parameters are similar to those typically used in modern XUV experiments [17]. The sample thickness amounts to 28.6 nm, which corresponds to the attenuation length (λ_{att}) of 50 eV photons in diamond [18]. This choice ensures an approximately uniform deposited dose across the simulated layer and a straightforward relation between incident fluence and absorbed dose. Moderate deviations from this particular thickness value are not expected to qualitatively affect the predicted polarization dynamics.

Optics EXPRESS

In our simulations, the probe (signal) pulse has a wavelength of $\lambda = 780$ nm. The optical response of irradiated diamond is calculated from the instantaneous complex dielectric function obtained at each time step (for details see the previous section). In order to account for the finite duration of the signal, a Gaussian temporal profile of the IR pulse was assumed, of a duration of 10 fs FWHM, and the calculated reflectivities were convolved with the profile. The convolution has been corrected for "edge" effects at the beginning and at the end of the simulation. The polarization angle rotation $\Delta\alpha'(t)$ was then evaluated directly from the convolved reflectivities.

Overall, we analyzed in our simulations a multivariate parameter space with: (i) the absorbed doses of XUV radiation between 0.16 eV/atom and 0.78 eV/atom, (ii) the incident angle of IR pulse, θ, between 25° and 65° (Brewster angle for ambient diamond, $\theta_B = 65°$), and (iii) the initial polarization angle of IR pulse, $\alpha = 10°, 45°, 80°$. In what follows we will present selected results relevant for the later discussion on the triggered 100-fs polarization change.

3.2. Refractive index

The base for the calculation of optical properties is the predicted complex refractive index. Figure 4 shows both the real (Fig. 4(a)) and imaginary (Fig. 4(b)) component of the refractive index, calculated for five different irradiation doses, 0.16-0.78 eV/atom. The temporal maximum of the XUV pulse intensity was at t=0 fs.

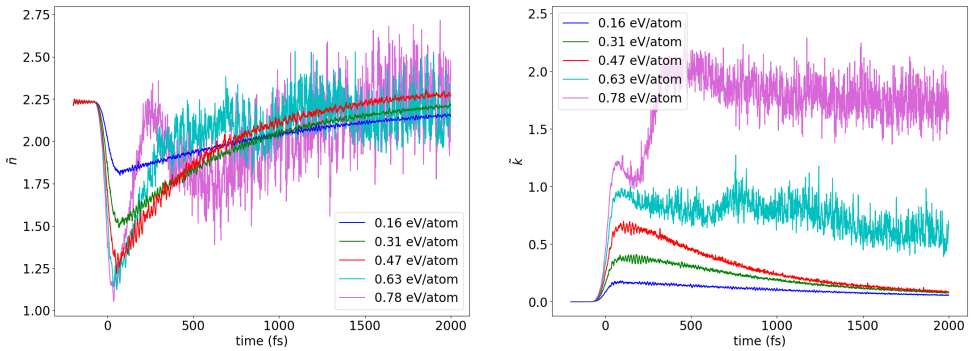

Fig. 4. Refractive index of the XUV irradiated diamond probed at 780 nm wavelength. It was calculated as a function of time at the absorbed radiation doses, 0.16 - 0.78 eV/atom. Both (a) real component $\tilde{n}$, and (b) imaginary component $\tilde{k}$ are shown. The maximum of XUV pulse intensity was at $t = 0$ fs. The simulations were performed using XUV pulse of 70 fs FWHM in duration, with photons of 50 eV energy. The supercell contained 216 atoms. The shape of the curves at the two highest absorbed doses indicate that a structural transition might be taking place.

For the three lowest absorbed doses in Fig. 4, both the real ($\tilde{n}$) and imaginary ($\tilde{k}$) components of the refractive index respond differently to the XUV pulse, with a characteristic initial decrease time ($\tilde{n}$) and increase time ($\tilde{k}$) of approximately 10 fs in duration. These short-time changes are due to the on-going electronic excitation. They are followed by a gradual recovery of the $\tilde{n}$ and $\tilde{k}$ to their initial values, occurring on a few-picosecond timescale. The recovery is stimulated by the electron-electron and subsequent electron-ion thermalization. Its occurrence is a prerequisite for optical switching applications, as the XUV induced changes in the material should be reversible. In contrast, the imaginary part of the refractive index ($\tilde{k}$) at the two highest absorbed doses (shown in Fig. 4) does not recover to its unpertubed value on a few picosecond timescale, indicating that the system has entered a regime in which the XUV radiation caused irreversible structural changes in diamond. These cases are discussed in detail in the Supplement 1, Sec. I. Simulations with additional intermediate dose values (not shown) showed that the "no-damage" regime extends for

Optics EXPRESS

absorbed doses up to about 0.60 eV/atom. The threshold dose is located between 0.60 eV/atom and 0.63 eV/atom. In what follows, we will focus only on the absorbed doses below the critical dose, in order to guarantee the full reversibility of the XUV induced optical changes.

Also, in order to obtain reliable predictions, we have to ensure that our XTANT simulations have converged in respect to the statistical simulation parameters such as the number of Monte Carlo iterations and the number of atoms in the simulation supercell. The latter has to be high enough to minimize the finite size effects. Regarding the statistical convergence of the Monte Carlo algorithm, the refractive-index curves obtained with 30,000 and 100,000 iterations are practically indistinguishable for all absorbed doses considered (see Supplement 1, Sec. II), indicating that the statistical uncertainty is below the plotting resolution. Regarding the supercell size convergence, if comparing 216-atom calculations with the 512-atom calculation as a reference, the simulation results differ for the doses of 0.16–0.47 eV/atom at t≥0 fs by 1.6–6.2% for $\tilde{n}$, and by 7.1–14.8% for $\tilde{k}$, with the corresponding absolute differences of 0.030–0.090 and 0.019–0.038, respectively (see Supplement 1, Sec. III). The larger relative deviations in $\tilde{k}$ are due to the small absolute magnitude of $\tilde{k}$ in this regime which is then stronger affected even by minor finite-size effects.

3.3. Reflectivity

Following the procedure described in the subsection 2.2, we calculated s- and p-reflectivities for IR wavelength of 780 nm. Figures 5 and 6 show the results obtained for the three "non-damaging" XUV absorbed doses and for seven different angles of incidence, θ. In order to account for the finite duration of the signal, a Gaussian temporal profile of IR pulse was assumed, of a duration of 10 fs FWHM, and the calculated reflectivities were convolved with that profile.

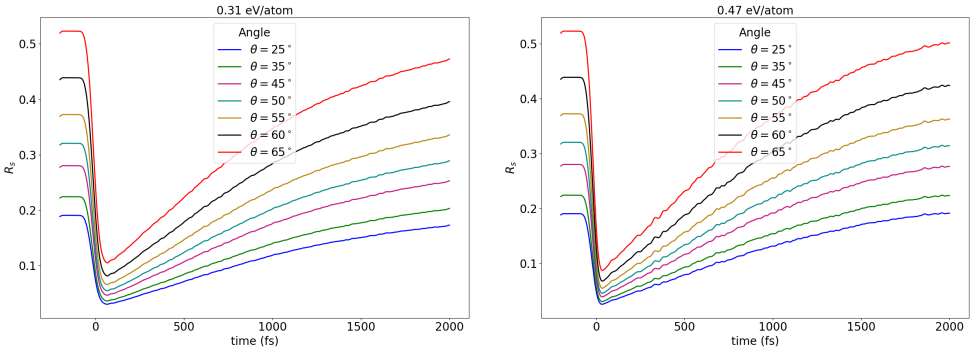

Fig. 5. Transient IR *s*-reflectivity of the XUV irradiated diamond calculated for different angles of incidence (25° - 65°) and two deposited doses: 0.31 eV/atom (left) and 0.47 eV/atom (right), convolved with the Gaussian temporal profile of the IR pulse of 10 fs FWHM in duration. Temporal maximum of the XUV pulse was at t = 0 fs. The simulations were performed using XUV pulses of 70 fs FWHM in duration. XUV photon energy was 50 eV. The supercell contained 216 atoms.

Initially, all the reflectivity curves show a rapid decrease on a sub-100-fs timescale comparable with the XUV pulse duration, except for the R_p curve that show a respective increase at the values of θ close to the Brewster angle ($\theta_B \approx 65°$ for ambient diamond [16]). The magnitude of the decrease depends on the absorbed dose. The sub-100-fs change of the reflectivities is followed by their slower recovery to the initial (unperturbed) value which takes around 2 ps. The observed trends are consistent with the temporal characteristics of the refractive index (Fig. 4). The temporal evolution of both reflectivity and refractive index thus reflects the timescales of microscopic processes in the irradiated diamond: the femtosecond carrier excitation and the

Optics EXPRESS

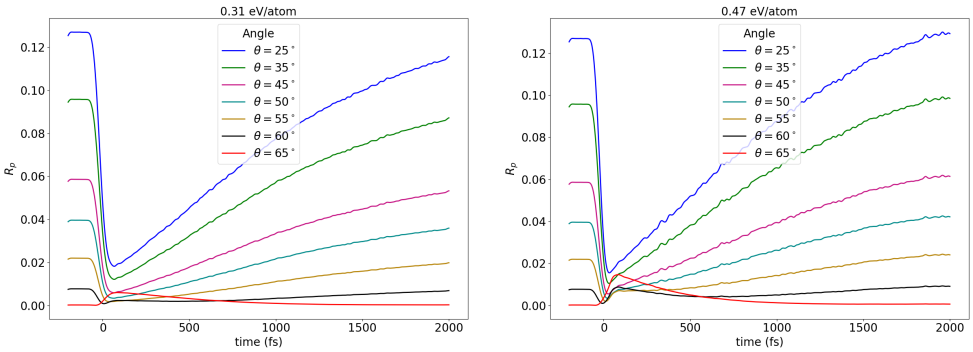

Fig. 6. Transient IR *p*-reflectivity of the XUV irradiated diamond calculated for different angles of incidence (25°-65°) and for two deposited doses: 0.31 eV/atom (left) and 0.47 eV/atom (right), convolved with the Gaussian temporal profile of the IR pulse of 10 fs FWHM in duration. Temporal maximum of the XUV pulse was at $t = 0$ fs. The simulations were performed using XUV pulses of 70 fs FWHM in duration. XUV photon energy was 50 eV. The supercell contained 216 atoms.

picosecond carrier–lattice relaxation. However, there is a distinct difference in the behaviour of R_p in respect to the trend observed in the refractive index at the values of θ close to the Brewster angle. This influences the transient behaviour of the IR pulse polarization which will be discussed in detail in the next subsection.

3.4. *Transient changes in optical polarization*

Using the results for R^s and R^p (convolved with the 10 fs FWHM IR pulse), we can obtain the predictions for the change of the polarization angle, $\Delta\alpha'(t)$ (Eq. (5)), calculated for the IR signal after its reflection from the XUV irradiated diamond. Figure 7 shows the predictions. The strongly non-linear behaviour of the $\Delta\alpha'(t)$ depends on the incidence angle, θ, and on the absorbed dose. For small incidence angles, $\theta = 25° - 35°$, $\Delta\alpha'(t)$ is initially decreasing on sub-100-fs timescale, and then it slowly recovers to zero value on a few picosecond timescale. Interestingly, for incident angles of 45° and 50° (Fig. 7 right) the initial dip becomes quite deep (of 13° depth). In case of $\theta = 45°$, it returns to a minus few degrees value on sub-100-fs timescale, in case of $\theta = 50°$, it slightly overshoots to a plus few degrees value. Both the dip and recovery occur on a 100-fs timescale. For the incident angles, $\theta \geq 55°$, the overshooting becomes stronger and stronger, reaching 40° at $\theta = 65°$. The cases presented in Fig. 7 were obtained for $\alpha = 80°$, i.e., for an almost p-polarized pulse. A qualitatively similar behavior has also been observed for other values of α (not shown), however, with lower magnitude of the initial $\Delta\alpha'(t)$ decrease.

The change of the polarization angle observed at $\theta = 45° - 50°$ at the dose of 0.47 eV/atom opens prospects for its potential practical applications. In this regime, we obtained a switching efficiency of approximately 13° and a switching time of about 100 fs at a control power of 800 GW/cm^2 (corresponding to the pulse fluence of 60 mJ/cm^2). Compared to previous polarization switching approaches summarized in Table 1, the predicted switching time is highly competitive. The higher control power required here reflects the radiation hardness of diamond and the absence of resonant field enhancement, as the mechanism relies only on the intrinsic electronic response of the bulk material following its XUV excitation.

Below we show the results obtained for $\theta = 45°$ at four deposited "non-damaging" doses of 0.16 eV/atom, 0.31 eV/atom, 0.39 eV/atom, and 0.47 eV/atom, covering the evolution time until 2 ps (Fig. 8). All curves exhibit a dip-and-recovery behavior. However, only for the highest non-damaging dose of 0.47 eV/atom, the dip and recovery of $\Delta\alpha'(t)$ occur within 100 fs, i.e., the

Optics EXPRESS

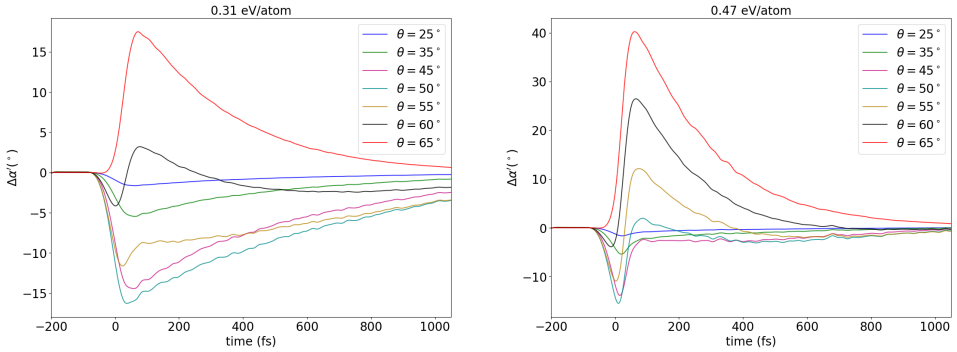

Fig. 7. Change of the polarization angle, $\Delta\alpha'(t)$ (Eq. (5)), calculated for the IR signal after its reflection from the XUV irradiated diamond. Various incidence angles (from 25° to 65°) were considered for two deposited doses: (right) 0.31 eV/atom, and (left) 0.47 eV/atom. The initial polarization angle was, $\alpha = 80°$. The simulations were performed using the XUV pulse of 70 fs FWHM in duration, with photons of energy of 50 eV. Temporal maximum of the XUV pulse was at $t = 0$ fs. The supercell contained 216 atoms. The plotted observable was calculated using the *p*- and *s*-reflectivities convolved with the Gaussian temporal profile of the IR pulse of 10 fs FWHM in duration.

polarization response no longer follows the two-picosecond relaxation timescales of the refractive index components $\tilde{n}$ and $\tilde{k}$. This 100 fs long dip-and-recovery is followed by a plateau lasting until approximately 500 fs before further relaxation proceeds. At 0.39 eV/atom, the early-time dynamics already exhibit the onset of a similar dip-and-recovery behaviour although overall, the two-picosecond recovery is still observed.

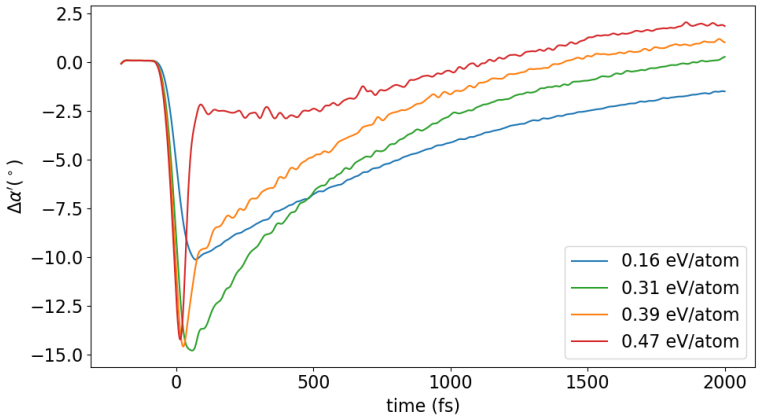

Fig. 8. Change of the polarization angle, $\Delta\alpha'(t)$, calculated for an IR signal after its reflection from the XUV irradiated diamond, for a nearly *p*-polarized pulse, $\alpha = 80°$. Four deposited doses of 0.16 eV/atom, 0.31 eV/atom, 0.39 eV/atom and 0.47 eV/atom were considered for a fixed incidence angle of 45°. The simulations were performed using the XUV pulse with photons of energy of 50 eV and 70 fs FWHM duration. The temporal maximum of the XUV pulse was at $t = 0$ fs. The supercell contained 216 atoms. The plotted observable was calculated using the *p*- and *s*-reflectivities convolved with the Gaussian temporal profile of the IR pulse of 10 fs FWHM in duration.

The results shown were obtained, using the *p*- and *s*-reflectivities convolved with the Gaussian temporal profile of the IR pulse of 10 fs FWHM in duration. We further examined the effect

Optics EXPRESS

of the probe pulse duration on the observed ultrafast feature by performing convolutions of the original results with longer probe pulses. As the probe duration increases, the dip-and-recovery feature in $\Delta\alpha'(t)$ becomes progressively less pronounced after the respective convolution (not shown). The feature practically disappears for probe pulse durations of 50 fs. The excitation parameters used in the simulations (reported in Sec. 3.1) correspond to those reported in Ref. [17], except that a higher pump intensity was assumed. The resulting control power lies within the range accessible in modern XUV pump–probe experiments at free-electron laser facilities. In practice, the main requirements for experimental observation of ultrafast polarization change are the generation of few-cycle probe pulses and a careful management of pump–probe timing jitter as well as of beam alignment, which can be routinely addressed.

The pronounced dip-and-recovery of the polarization angle is a consequence of the interplay between the p- and s-components of transient reflectivity, because the change of the polarization angle of the reflected signal depends on the R_p/R_s ratio (see Eqs. 4 and 5). Figure 5 shows that R_s component of reflectivity at various incidence angles changes as a function of time in a similar way for the doses of 0.31 eV/atom and 0.47 eV/atom, always with a characteristic dip and the following recovery towards its original (unperturbed) value. However, Fig. 6 shows that this is not the case for the R_p component. Here, at the incidence angle value of 45° the slope of the reflectivity curve starts to flatten after the initial dip. This effect becomes stronger with increasing incidence angle, which at at the angle of 60° finally leads to a pronounced change of the shape of the reflectivity curve. Namely, it then initially increases to a peak value and later decreases to its initial value. The observed dip-and-recovery of the polarization angle results from this strongly non-linear transition in the behaviour of R_p. Flattening of slope of the reflectivity curve as a function of time after the initial dip leads to the rapid decrease of $\Delta\alpha'(t)$ value on 100 fs timescale. The simulations show that the changes of R_p are most pronounced for the dose of 0.47 eV/atom, and this triggers the ultrafast dip-and-recovery of $\Delta\alpha'(t)$ at this dose value (Fig. 7).

The prediction that the ultrafast $\Delta\alpha'(t)$ change is markedly shorter than the intrinsic carrier relaxation times governing the recovery of $\tilde{n}$ and $\tilde{k}$ demonstrates that the signal polarization can change in a controllable way faster than the scalar optical constants themselves. Such a rapid $\Delta\alpha'(t)$ recovery in XUV-driven diamond (reported here for the first time) indicates that the polarization switching in wide-bandgap semiconductors can be decoupled from carrier thermalization, thus opening a possible pathway to 100-fs polarization control.

4. Conclusion

We have investigated the ultrafast optical response of diamond irradiated by intense femtosecond XUV pulses, using the XTANT code, which tracks electronic excitation, atomic motion, and calculates transient optical properties. Below the structural-damage threshold, the transient interplay between the refractive and absorptive components of the complex refractive index can produce a distinct 100 fs dip and recovery of the reflected polarization. This ultrafast polarization change, of several degrees in-depth, recovers faster than the intrinsic carrier relaxation timescale of the material. We determined the optimal conditions to trigger the 100 fs polarization change in diamond by systematically varying the absorbed XUV dose and IR probe incidence geometry. Since this change arises solely from the electronic response to XUV irradiation and does not involve any structural modification of the irradiated material, it establishes a reversible, damage-free pathway for 100 fs polarization modulation in wide-bandgap semiconductors. Profiting from uniform dose deposition and accurate dose control within the irradiated volume in the XUV regime, the excitation remains confined to the electronic subsystem only. Experimental verification of our predictions through dedicated time-resolved polarization measurements, with free-electron lasers (FELs) or high-harmonic generation sources, synchronized with low-jitter infrared (IR) sources, could help to utilize this unique feature for the construction of compact XUV-optical polarization modulators, integrated into tabletop laser setups.

Optics EXPRESS

Acknowledgment. The authors thank Victor Tkachenko for fruitful discussions.

Disclosures. The authors declare no conflicts of interest.

Data availability. Data underlying the results presented in this paper are not publicly available at this time but may be obtained from the authors upon reasonable request.

Supplemental document. See Supplement 1 for supporting content.

References

1. D. Hui, H. Alqattan, S. Zhang, *et al.*, "Ultrafast optical switching and data encoding on synthesized light fields," Sci. Adv. **9**(8), eadf1015 (2023).
2. Z. Chai, X. Hu, F. Wang, *et al.*, "Ultrafast all-optical switching," Adv. Opt. Mater. **5**(7), 1600665 (2017).
3. X. Niu, X. Hu, Y. Xu, *et al.*, "Ultrafast all-optical polarization switching based on composite metasurfaces with gratings and an epsilon-near-zero film," Adv. Photonics Res. **2**(4), 2000167 (2021).
4. H. Wang, Z. Hu, J. Deng, *et al.*, "All-optical ultrafast polarization switching with nonlinear plasmonic metasurfaces," Sci. Adv. **10**(8), eadk3882 (2024).
5. K. Xu, B. Y. Zhang, Y. Hu, *et al.*, "A high-performance visible-light-driven all-optical switch enabled by ultra-thin gallium sulfide," J. Mater. Chem. C **9**(9), 3115–3121 (2021).
6. X. Dong, Y. He, R. Gao, *et al.*, "Plasmonic ultrafast all-optical switching with a superior on-off ratio," Nano Lett. **25**(10), 4005–4012 (2025).
7. L. H. Nicholls, F. Rodriguez Fortuno, M. Nasir, *et al.*, "Ultrafast synthesis and switching of light polarization in nonlinear anisotropic metamaterials," Nat. Photonics **11**(10), 628–633 (2017).
8. P. Rupprecht, D. M. Neumark, and S. R. Leone,"All-optical logic gates for extreme ultraviolet switching via attosecond four-wave mixinge," arXiv (2025).
9. M. Kozák, F. Trojánek, and P. Malý, "Hot-carrier transport in diamond controlled by femtosecond laser pulses," New J. Phys. **17**(5), 053027 (2015).
10. N. Medvedev, H. O. Jeschke, and B. Ziaja, "Nonthermal graphitization of diamond induced by a femtosecond x-ray laser pulse," Phys. Rev. B **88**(22), 224304 (2013).
11. N. Medvedev, V. Tkachenko, V. Lipp, *et al.*, "Various damage mechanisms in carbon and silicon materials under femtosecond x-ray irradiation," 4open **1**, 3 (2018).
12. V. Lipp, V. Tkachenko, M. Stransky, *et al.*, "Density functional tight binding approach utilized to study x-ray-induced transitions in solid materials," Sci. Rep. **12**(1), 1551 (2022).
13. F. Tavella, H. Höppner, V. Tkachenko, *et al.*, "Soft x-ray induced femtosecond solid-to-solid phase transition," High Energy Density Phys. **24**, 22–27 (2017).
14. S. Antunes, M. Stransky, V. Tkachenko, *et al.*, "Calculation of effective pump dose in X-ray-pump/X-ray-probe experiments," J. Synchrotron Radiat. **32**(5), 1106–1115 (2025).
15. V. Tkachenko, N. Medvedev, Z. Li, *et al.*, "Transient optical properties of semiconductors under femtosecond x-ray irradiation," Phys. Rev. B **93**(14), 144101 (2016).
16. P. Yeh, *Optical Waves in Layered Media*, (Wiley, 2005), chap. 3, Wiley Series in Pure and Applied Optics.
17. R. Mincigrucci, F. Bencivenga, E. Principi, *et al.*, "Timing methodologies and studies at the FERMI free-electron laser," J. Synchrotron Radiat. **25**(1), 44–51 (2018).
18. B. L. Henke, E. M. Gullikson, and J. C. Davis, "X-ray interactions: Photoabsorption, scattering, transmission, and reflection," https://henke.lbl.gov/optical_constants/atten2.html (1993). Accessed: 2025-07-01.